Tandem structured quantum dot/rod sensitized solar cell based on solvothermal synthesized CdSe quantum dots and rods

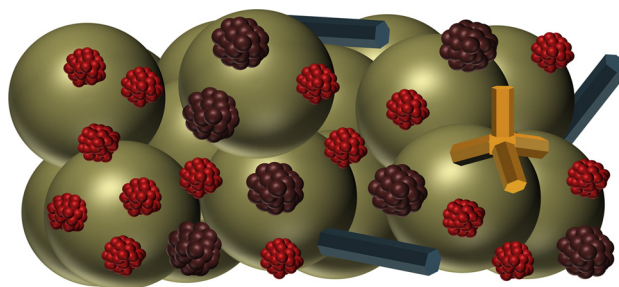Mohammad Reza Golobostanfard [a],[*], Hossein Abdizadeh [a],[b]

[a] School of Metallurgy and Materials Engineering, College of Engineering, University of Tehran, P.O. Box 14395-553, Tehran 1937676316, Iran
[b] Center of Excellence for High Performance Materials, University of Tehran, Tehran, Iran

HIGHLIGHTS

- Quantum dots of different sizes and shapes were synthesized by solvothermal method.
- Tandem structured quantum dots/rods were formed on hierarchical porous anode by electrophoretic.
- Cell efficiency was dramatically improved in tandem structured solar cell.
- Quantum rods greatly enhanced the charge separation and electron lifetime.

GRAPHICAL ABSTRACT

ARTICLE INFO

ABSTRACT

The quantum dots (QD) and quantum rods (QR) of different sizes, shapes, and crystalline phases are synthesized by modified solvothermal method spontaneously employed stirring system and controlled internal applied pressure. The tandem structure of QDs and QRs as well as tetrapods is formed on hierarchical porous titania photoanode by means of electrophoretic deposition. A tremendous enhancement in efficiency of the cell is obtained in samples synthesized at 220 °C for 24 h due to the formation of tandem structure, utilization of Cu_2S/CNT composite cathode, co-sensitization of CdS and CdSe, and beneficial role of QRs in electron lifetime. Smaller size QDs with higher band gaps penetrate deeper through the macro-channels of the hierarchical porous structure, while the QRs and tetrapods with lower band gaps are placed on upper layers. Although the charge injection is improved in smaller QDs, the electron lifetime in QRs is longer mainly due to the higher absorption cross section, proper charge separation, introduction of quasi-one dimensional route for charge transport through QRs, and higher surface area available for regeneration with electrolyte. The cell shows the efficiency of 1.05% with J_{SC} of 4.48 mA cm^{-2}, V_{OC} of 0.45 V, and fill factor of 0.52.

1. Introduction

Dye sensitized solar cells (DSSC) have attracted a great deal of attention in recent years due to the relatively high efficiency, low fabrication cost, functioning at both direct and diffuse light, and flexibility in shape, color, and transparency [1,2]. However, further improvement in efficiency and stability of these cells is needed through overcoming the bottlenecks such as volatility of the electrolyte, nearly narrow absorption range, and low molar extinction coefficient of the dye [3—5]. Quantum dot sensitized solar cells (QDSC) are of great interest due to the possibility of boosting the energy conversion efficiency beyond the thermodynamic Shockley—Queisser limit [6]. Semiconductor quantum dots (QD) as light harvesters in solar cells have the advantages of (1) higher molar extinction coefficient, (2) size tunable band gap, and (3) ability for

* Corresponding author. Tel.: +98 9122300382; fax: +98 21 88006076.
E-mail addresses: Bostanfr@ut.ac.ir, Mohammadreza.Golbostanfard@gmail.com (M.R. Golobostanfard).

hot electron utilization and multi-exciton generation compared to molecular dye used in DSSCs [7–9].

Although the efficiency of the QDSCs has reached so far to 5.6% [10], further improvement in efficiency of these cells should be obtained in order to make these devices commercially attractive. The major bottlenecks in these devices include porous photoanode morphology which should be optimized for deep penetration of larger size QDs compared to molecular dye [11], back reaction recombination at TiO$_2$/QD/electrolyte interface due to low surface coverage and short electron lifetime [12], finding suitable electrolyte with high stability and high QD regeneration efficiency without affecting the open-circuit voltage [13], proper counter electrode fitted to the electrolyte [14], and TiO$_2$/QD attachment and interface [15]. The tandem structure (rainbow structure) is the amazing strategy to increase the photovoltaic cell performance with utilization of various band gap semiconductors in series configuration to extend the absorption region. This strategy gains the world record efficiency for photovoltaic devices reaching the efficiency of 42.3% in GaAs three junction based cell [16]. The tandem structure was also utilized in DSSC [17] with different dyes and QDSC [18] with CdSe$_{1-x}$S$_x$ compounds.

Photoanodes of QDSCs are usually sensitized by QDs with two different approaches: (1) pre-synthesized QDs were prepared generally by hot injection method attached to TiO$_2$ surface by direct deposition [19], linker assisted attachment [20], or electrophoretic deposition [21] and (2) in-situ synthesis of QDs directly onto TiO$_2$ surface with successive ionic layer adsorption and reaction (SILAR) [22] or chemical bath deposition [23]. The former approach has the advantages of controllable size of the QDs and high crystallinity. However, the latter methods lead to high surface coverage. The attachment of the pre-synthesized QDs with electrophoretic deposition leads to higher performance than linker assisted or direct attachment methods due to the band gap tailoring occurs in linker assisted attachment or weak binding exists in direct attachment.

The shape and crystalline phases of QDs can be controlled more simply in solvothermal method compared to conventional hot injection method [24–26]. Moreover, the capping molecules used in hot injection method for controlling the size of QDs strongly affect the band edge position of QDs [27]. Nevertheless, the size distribution in this method is wider than in hot injection [28,29].

In this article, the hierarchical porous titania photoanodes, which offer the high surface area of mesoporosities for QD and quantum rods (QR) adsorption together with large channels of macroporosities suitable for QD and QR impregnation, were synthesized through phase separation method. These ordered porous structures have the advantages of very low residual organic species, ability to easily control and design the pore size distribution and dimension, and possibility to synthesize inter-connected thick porous films compared to soft or hard templating methods [30]. The CdSe QDs and QRs were prepared with modified solvothermal method in various sizes, shapes, and crystalline phases. The co-sensitization of the photoanode with CdS and CdSe as well as the tandem sensitizations with QDs of different sizes and QRs by means of electrophoretic deposition were considered and the effects of different QD and QR sizes, shapes, and crystalline phases on QDSC device performance were investigated.

2. Experimental

2.1. Material

Cadmium oxide powder (CdO), cadmium nitrate (Cd(NO$_3$)$_2$), selenium chloride (SeCl$_4$), triethylene tetramine (TETA), ethanol (EtOH), 1-propanol (1PrOH), hydrochloric acid (HCl), tetrapropyl ortotitanate (TTiP), tetrabutyl ortotitanate (TBT), diethanol amine (DEA), polyethylene glycol (PEG, average molecular weight 1000), sulfur powder (S), sodium sulfide (Na$_2$S), sodium hydroxide (NaOH), zinc acetate dehydrate (ZAD), and copper chloride (CuCl$_2$) were all in reagent grade and purchased from Merck. Deionized water (DIW) was used in all experiments. The fluorine doped tin oxide conductive glass substrates (FTO, 15 Ω □$^{-1}$) and Surlyn ionomer were purchased from Dyesol. Carbon nanotubes (MWCNT, outer diameter 40–60 nm, 97% purity, 130–160 m^2 g^{-1}) were provided from Shenzen Nanotech port. All chemicals were used as received without further purification. It should be noted that the cadmium and selenium compounds are extremely hazardous.

2.2. CdSe quantum dot synthesis

In this research, CdSe QDs were synthesized by modified homemade solvothermal reactor, which utilized the stirring system and controlled internal pressure. The reactor is schematically shown in Fig. 1. Typically, 1 mmol of CdO powder and 1 mmol of SeCl$_4$ were dissolved in 20 mL TETA in the solvothermal reactor. The external pressure of 400 kPa was applied to the reactor and the reactants were heated at 220 °C for 24 h under continuous stirring. Then, the precipitates were separated and centrifuged at the speed of 14,000 rpm and redispersed in ethanol. The centrifugation and dispersion process was repeated several times to ensure removal of organic residues. Finally, stepwise size selective centrifugation was applied to obtain CdSe quantum dots. The synthesis temperature of 180 and 260 °C and synthesis time of 1, 2, and 12 h were also considered. In all experiments while one parameter was changed, the other parameters were held constant.

2.3. Photoanode preparation

The photoanode contains two different titania layers: a very thin dense blocking layer and a hierarchical porous thick layer. The FTO substrates were cleaned ultrasonically in detergent solution, DIW, and EtOH for 10 min. The titania sol was prepared based on synthesis route discussed elsewhere [31]. Briefly, 1 mmol TTiP was dissolved in 38 mmol 1PrOH. The hydrolyzing solution containing 4.5 mmol DIW, 0.5 mmol HCl, and 38 mmol 1PrOH was added dropwisely to the former solution to obtain the transparent stable sol. The prepared sol was spin coated on FTO substrates at the speed of 3000 rpm for 30 s and dried at 100 °C for 10 min. The spin coating
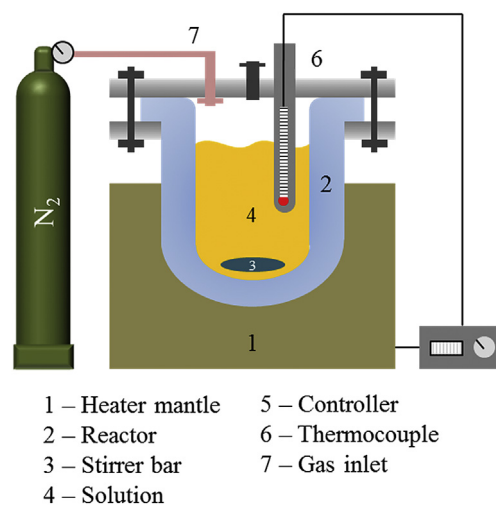

1 – Heater mantle   5 – Controller
2 – Reactor   6 – Thermocouple
3 – Stirrer bar   7 – Gas inlet
4 – Solution

Fig. 1. Schematic representation of the designed reactor.

and drying process was repeated twice to reach the thickness of about 100 nm. Then, the film was calcined at 450 °C for 1 h. This very thin layer was applied as a blocking layer in photoanode.

For preparing the hierarchical porous layer, another sol was synthesized according to the previous research [32]. Typically, 1 mmol TBT was dissolved in 10 mmol EtOH and stirred for 30 min. 1 mmol DEA was added to the solution and stirred for 1 h. The hydrolyzing solution containing 1 mmol DIW in 7 mmol EtOH was added drop-wisely to the TBT solution and stirred for 30 min. Then, 1 g L^{-1} PEG was added to the resultant sol and stirred for another 1 h. The sol was kept for 2 h and then deposited on coated FTO substrates with dip coating method at the speed of 60 mm min^{-1} and dried at 300 °C for 10 min. The process of dip coating and drying was repeated 50 times to obtain a thickness of about 10 μm. Finally, the films were annealed at 550 °C for 1 h. This layer acts as both porous and scattering layers.

2.4. Solar cell fabrication

The photoanode was sensitized by CdSe QDs with electrophoretic deposition. For this purpose, first a CdS layer was deposited on photoanodes through SILAR. 0.05 M Cd(NO$_3$)$_2$ in EtOH and 0.05 M Na$_2$S in DIW and MeOH were used as the cationic and anionic solutions, respectively. Each SILAR cycle contains dipping the photoanode in cationic and anionic solutions for 1 min and then rinsing with corresponding solvent followed by air drying. Four SILAR cycles were deposited on photoanodes. The 2 mM stable dispersion of CdSe QDs in EtOH was deposited on FTO/TiO$_2$/CdS photoanode by electrophoretic deposition with applying 150 V cm^{-1} for 1 h. Finally, a very thin ZnS barrier layer was deposited on photoanodes by SILAR method. The 0.1 M ZAD in DIW and 0.1 M Na$_2$S in DIW were used as cationic and anionic solutions, respectively. Two SILAR cycles were applied on the photoanodes.

The polysulfide electrolyte was 1 M Na$_2$S, 1 M S, and 0.1 M NaOH in DIW. The counter electrode was also prepared by SILAR deposition of Cu$_2$S on MWCNT coated FTO substrates. 25 g L^{-1} functionalized MWCNT dispersion in EtOH was deposited on cleaned FTO substrate through electrophoretic deposition in 50 V cm^{-1} for 2 min. Next, SILAR of Cu$_2$S was performed by using 0.2 M CuCl$_2$ in DIW and 0.1 M Na$_2$S in DIW for cationic and anionic solutions, respectively. Four SILAR cycles were applied on FTO/MWCNT electrodes.

The cell was fabricated based on sandwich type cell with FTO/TiO$_2$/CdS/CdSe/ZnS photoanode and FTO/MWCNT/Cu$_2$S cathode and sealed by Surlyn ionomer. The electrolyte was injected into the cell by evacuation through predrilled hole. Then, the hole was sealed by Surlyn and microscope glass slide. The active area of TiO$_2$ photoanode was 0.16 cm^2.

2.5. QD and solar cell characterization

X-ray diffraction (XRD), Philips X-pert pro PW1730, Cu-Kα, was utilized to study the phase structure of the photoanodes. High resolution transmission electron microscope (HRTEM), Philips CM30, 250 kV, equipped with selected area electron diffraction pattern (SAED) was employed to study the QD morphologies and crystalline phases. Field emission scanning electron microscopy (FESEM), Hitachi S4160, was used to investigate the morphology of porous films. Atomic force microscopy (AFM), Dual Scope DS 95-200/50, was performed in contact mode to achieve surface roughness of the films. The infrared spectra were recorded using Fourier-transformed infrared (FTIR) spectrophotometer, Bruker TENSOR27, in transmittance mode at 400–4000 cm^{-1} with KBr as blank. Diffuse reflectance spectroscopy (DRS), Avalight DH-S Avaspec 2048 TEC, was performed to investigate the absorption

and band gap of the QDs. The spectra were calibrated with Kubelka–Munk function: $F(R) = (1 - R^2)/2R$, where $F(R)$ and R are equivalent absorption coefficient and reflectance, respectively. Raman spectra were recorded using BRUKER (SETERRA, spectral resolution <3 cm^{-1}) micro Raman spectrometer equipped with the confocal microscope. The excitation wavelength was 785 nm line of argon laser operating at the power of 25 mW. Photovoltaic measurements were performed using an AM1.5 solar simulator. The power of simulated light was calibrated to 1000 W m^{-2} with Si photodiode. J–V curves were obtained by applying an external bias to the cell and measuring the generated photocurrent with a PGSTAT digital source meter. All the tests were conducted in room temperature. For repeatability test, two cells with the same conditions for each parameter were fabricated. The incident photon to current conversion efficiency (IPCE) was carried out with spectral response measuring equipment Keithley 2000 multimeter under the illumination of a 150 W tungsten lamp with a monochromator. The reference cell for IPCE measurement was IR-cut crystalline silicon cell. Electrochemical impedance spectra of QDSCs were recorded using a Potentiostat EG&G 273A analyzer. The obtained impedance spectra were fitted with Z-view software. The spectra were measured under AM1.5 illumination condition and in the frequency range of 0.1 Hz–1 MHz with oscillation potential amplitudes of 10 mV at room temperature.

3. Results and discussion

3.1. QD and QR characterization

The XRD patterns of CdSe powders synthesized at different temperatures of 180, 220, and 260 °C for 24 h before size selective centrifugation are shown in Fig. S1(a) (see Supplementary data). The patterns confirm the formation of wurtzite (WZ) CdSe (JCPDS 08-0459) and zinc blende (ZB) CdSe (JCPDS 19-0191) in all samples. Unreacted cadmium (JCPDS 05-0674) could be detected in sample synthesized at 180 °C. Thus, this temperature is not suitable for synthesis of CdSe QDs. Since most of the diffraction peaks of ZB and WZ structures overlap with each other, the amounts of these phases can be roughly estimated by calculating the (103) WZ to (220) ZB peak intensity ratio. This ratio is equal to 0.28, 0.32, and 0.4 for synthesis temperature of 180, 220, 260 °C, respectively, which represents that the WZ to ZB phase ratio increases with increasing the reactor temperature. There is a very strong coordination interaction between TETA and Cd^{2+} due to the quite large cumulative formation constant (log K) [33]. Therefore, the Cd-(TETA^{3+})$_2$ species were formed in the reactor, which totally reduces the Cd^{2+} ions concentration, and hence decreases the rate of CdSe formation. Thus, thermodynamically stable WZ phase can be formed in higher synthesis temperature. On the other hand, kinetically stable ZB phase is dominant in lower synthesis temperature.

The XRD patterns of CdSe powders synthesized at 220 °C for 1, 2, 12, and 24 h are illustrated in Fig. S1(b) (Supplementary data). Crystalline WZ and ZB CdSe phases are again formed in all samples. However, it seems that the synthesis time of 1 h is inadequate, where some unreacted cadmium could be detected in this sample. The WZ to ZB ratio is 0.28, 0.19, 0.20, and 0.32 for synthesis time of 1, 2, 12, and 24 h, respectively. The presence of unreacted Cd in synthesis time of 1 h causes higher WZ to ZB ratio. However, this ratio is enhanced with synthesis time in other samples.

The Raman spectrum of the CdSe powder synthesized at 220 °C for 24 h is indicated in Fig. 2(a). The Raman spectrum of CdSe involves TO (175.8 cm^{-1}), SO (195.0 cm^{-1}), LO (207.9 cm^{-1}), LO + TA (225.1 cm^{-1}), LO + LA (235.6 cm^{-1}), LO + Γ$_6$ (248.4 cm^{-1}), 2TO (356.8 cm^{-1}), TO + LO (377.4 cm^{-1}), SO + LO (395.0 cm^{-1}), and 2LO
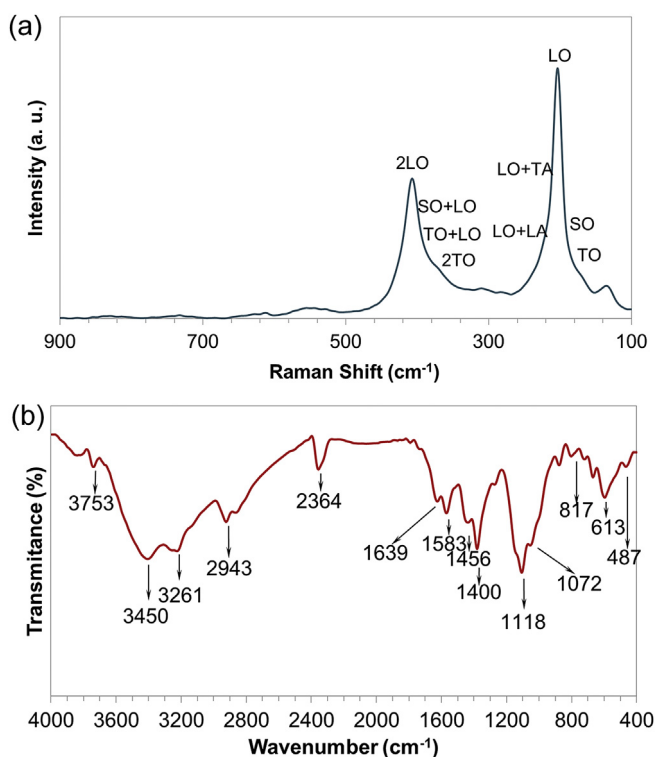
Fig. 2. (a) Raman spectrum and (b) FTIR spectrum of the CdSe powder synthesized at 220 °C for 24 h.

(415.6 cm^{-1}) modes [34]. The Raman spectrum confirms the formation of CdSe (mostly in ZB structure in this sample).

The FTIR spectrum of the CdSe QDs synthesized at 220 °C for 24 h is presented in Fig. 2(b). The peaks around 3753, 3450, 1118, and 1072 cm^{-1} are assigned to free O–H, O–H stretching, O–H bending, and CH_2–OH, respectively. Also, the peaks around 3600, 3530, 2364, 1639, 1583, 1350, 817, and 613 cm^{-1} are corresponded to the C–N (NH_2), C–N (NH), NH^+ stretching, NH_2^+ bending, aryl stretching, C–N (NH_2) bending, and CH_2–NH–CH_2, respectively. The C–H and CH_2/CH_3 bending bonds could be detected at around 2943 and 1400 cm^{-1}, respectively. The FTIR spectrum of QDs confirms a trace amount of hydroxyl and amino groups on the surface of QDs after size selective separation.

HRTEM micrographs of the CdSe samples synthesized at 220 °C for 2 and 24 h are shown in Fig. 3(a) and (c), respectively. QDs with the diameter of about 6 nm and aspect ratio of about 2 are formed in the synthesis time of 2 h. The HRTEM micrograph in Fig. 3(b) indicates the formation of WZ phase inside the ZB structure in this sample. A very high coherence interface between planes of (111) in ZB and (002) in WZ structure results in the formation of WZ phase in some region. However, the QRs with diameter of about 6–8 nm and length of about 46–78 nm are formed in longer synthesis time. The lattice fringes of c-axis (002) planes of WZ structure are shown along the rod length in Fig. 3(d). The synthesis time of 12 h leads to the shorter QRs with lengths of about 22–55 nm (not shown). A slightly larger QDs also exist in both synthesis time of 12 and 24 h. Moreover, the tetrapods could be detected in some regions in synthesis time of 24 h (Fig. 3(f)). The SAED pattern of the QDs synthesized for 2 h is illustrated in Fig. 3(e). It could be inferred that the QDs are almost single crystalline ZB structure.

The formation of QRs in longer synthesis time could be explained by three main reasons: (1) QDs are formed in low growth rate regime; (2) QRs are mostly synthesized in high growth rate regime; (3) amines are attached to the non-polar lateral planes of

WZ structure and stabilize the rods along c-axis [29,35]. The amine as a solvent such as TETA also strongly reacts with Cd^{2+} ions and reduces the concentration of these ions in the reactor, which further results in kinetically stable ZB phase. Nevertheless, the thermodynamically stable phase of WZ is formed in longer synthesis time. Furthermore, it should be mentioned that the CdSe crystal has no inverse symmetry, which means that the (001) and ($00\bar{1}$) planes are not the same [36]. Thus, the growth rate of ($00\bar{1}$) is higher in the presence of TETA. Tetrapods are also formed through formation of initial ZB nuclei. Then, four arms form on the {111} faces of ZB structure and grow along the (002) planes of WZ, forming the tetrapod shapes [37].

The DRS spectra of the CdSe QDs and QRs synthesized at 220 °C for 2 and 24 h are demonstrated in Fig. 4. The band gap of 1.77 and 1.75 eV could be obtained for QDs synthesized for 2 and 24 h, respectively. Since the band gap of CdSe in bulk form is equal to 1.74 eV, the higher band gap values in these samples are due to the quantum confinement effect according to the Eq. (1) [38].

$$\Delta E = \frac{\hbar^2 \pi^2}{2R^2} \left(\frac{1}{m_e^*} + \frac{1}{m_h^*} \right) - \frac{1.8 e^2}{\varepsilon R} \tag{1}$$

where ΔE is change in band gap, $\hbar$ is Plank's constant, m_e^* is electron effective mass, m_h^* is hole effective mass, ε is dielectric constant, and R is the radius of the particles. In QDs, the band gap of smaller particles blue shifts toward higher energies. In case of QRs, the wave function distribution concentrates inside the rod, so the eigen energy values are determined mostly by the rod dimensions. When the rod diameter is small enough in comparison with its length, the rod resembles a nanowire where the confinement effect is dominated by the rod diameter only. When the arm diameter turns comparable to its length, both the diameter and length affect the confinement effect [37]. It should be noted that the organic ligands remained from synthesis and size selective separation processes can strongly affect the band edges of the material in both cases (QDs and QRs). Consequently, the blue shift of band gap occurs in both cases especially in QDs.

3.2. Photoanode characterization

The hierarchical porous photoanodes were synthesized by sol–gel induced phase separation. In this method, the macropore sizes can be truly controlled by the sol and deposition parameters [32]. These parameters were chosen in a way that the lowest possible size of macropores with proper inter-connectivity were formed appropriate for QDSC. The mesopores in these structures are formed during calcination and crystallization. This template free method offers low levels of organic residues, which is beneficial for charge injection and transfer in the device. The FESEM and AFM images of the hierarchical porous photoanode were illustrated in Fig. 5. The mesopore, macropore, and particle sizes of about 15, 350, and 25 nm with very narrow size distribution are formed in the film, respectively (Fig. 5(a)). The thickness of the porous photoanode is about 11.5 μm after 50 times deposition (Fig. 5(b)). Also, it could be inferred from Fig. 5(c) that the surface roughness, root mean square, and mean peak to valley of the photoanode are about 15.4, 19.1, and 134 nm, respectively. Since the thickness of each layer is more than 230 nm and the AFM was performed in non-contact mode, the depth of macro-channels might be higher than reported 134 nm.

3.3. QDSC characterization

In QDSCs used in this study, there are so many fixed components including type and thickness of blocking layer (titania compact
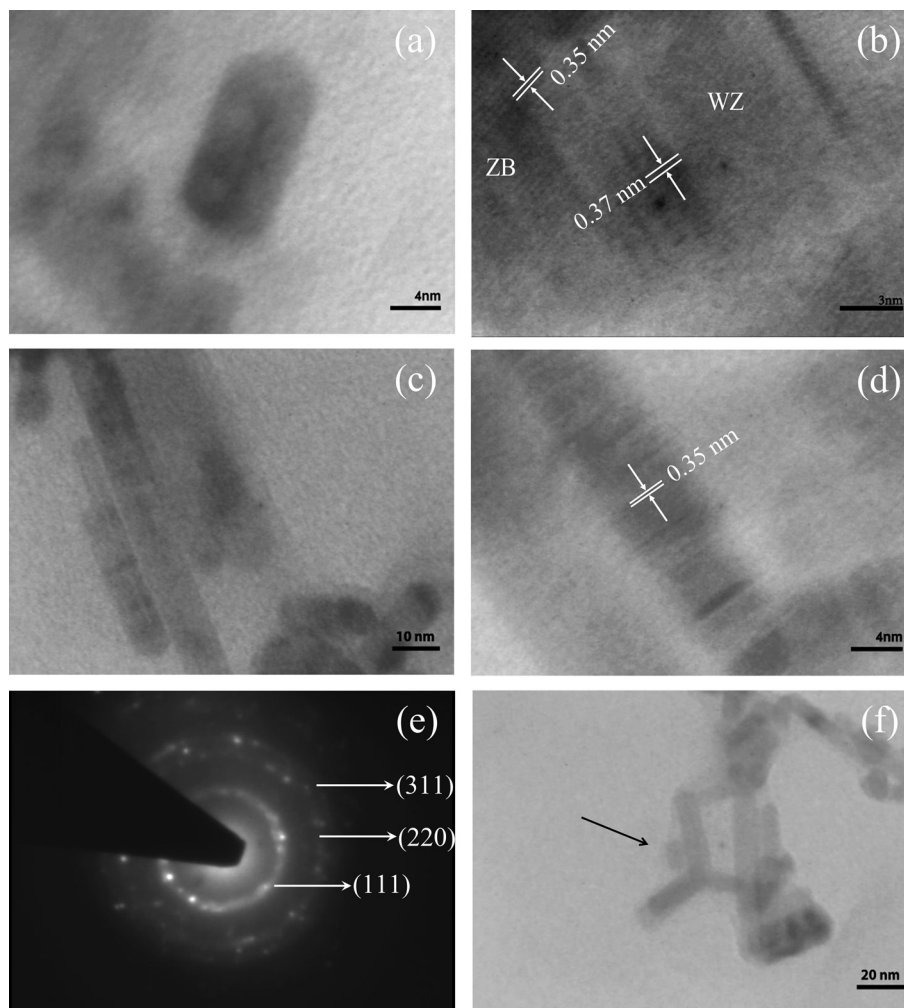
Fig. 3. HRTEM micrographs of the CdSe QDs and QRs for samples synthesize at 220 °C (a) for 2 h, (b) higher resolution of (a), (c) for 24 h, (d) higher resolution of (c), (e) SAED pattern of QD from (a), and (f) a tetrapod detected in (b).

layer with thickness of about 100 nm to prevent recombination at substrate/electrolyte interface), type, morphology and thickness of hierarchical porous photoanode (titania porous layer with thickness of about 10 μm for charge transfer and sensitizer scaffold), type of QDs (solvothermal synthesized CdSe), type and thickness of co-sensitizer (four SILAR layers of CdS), type and thickness of barrier

Fig. 4. DRS spectra of the CdSe QDs and QRs synthesized at 220 °C for 2 and 24 h.

layer (two SILAR layers of ZnS), type of electrolyte (polysulfide electrolyte), and type of counter electrode (CNT/Cu_2S composite counter electrode). The only varied component in QDSCs is the size and shape of QDs, which can be strongly affected by altering the synthesis time.

The short circuit current density–open circuit voltage characteristic and IPCE curves of the QDSCs with different QDs synthesized in different times are represented in Fig. 6. The short circuit current density (J_{SC}), open circuit voltage (V_{OC}), fill factor (FF), and efficiency (η) of each cell are also shown in Table 1. The highest efficiency is achieved in 24 h synthesized sample, which is mainly resulted from high J_{SC}. The QDs synthesized for 1 and 2 h are mainly comprised of very small QDs. However, samples synthesized for 12 and 24 h contained QRs and tetrapods besides QDs of different sizes.

The higher efficiency in QDSC with 24 h synthesized QDs can be explained by assuming four main reasons: (1) size effect; (2) shape effect; (3) CdS co-sensitization and ZnS blocking layer; and (4) the electrolyte and redox couples. It is well known that the QDs with different sizes undergo a different band widening in a way that the smaller particles have larger band gaps and the most changes occur in conduction band (CB) of the semiconductor due to the lower effective mass of electrons [39]. Thus, smaller QDs absorb higher energy photons and inject excited electrons faster into the CB of TiO_2.
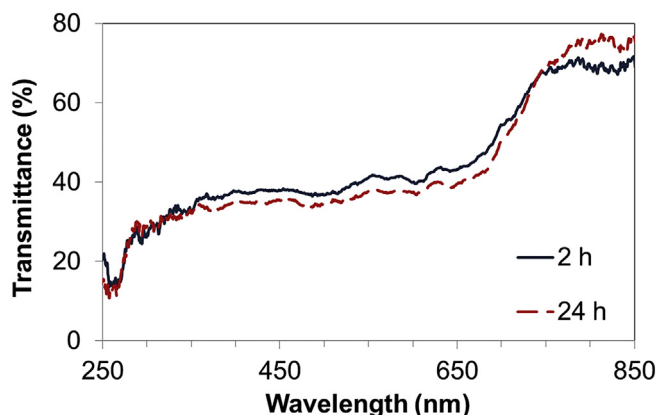
The QRs can be mainly blamed for the appearance of shape effect in this cell. QRs and tetrapods show lower quantum confinement effect due to the larger size. Therefore, they can absorb lower energy photons. Also, QRs and tetrapods with larger volumes than QDs have significantly larger absorbance cross section per particle [40]. Moreover, electron and hole wave functions are separated
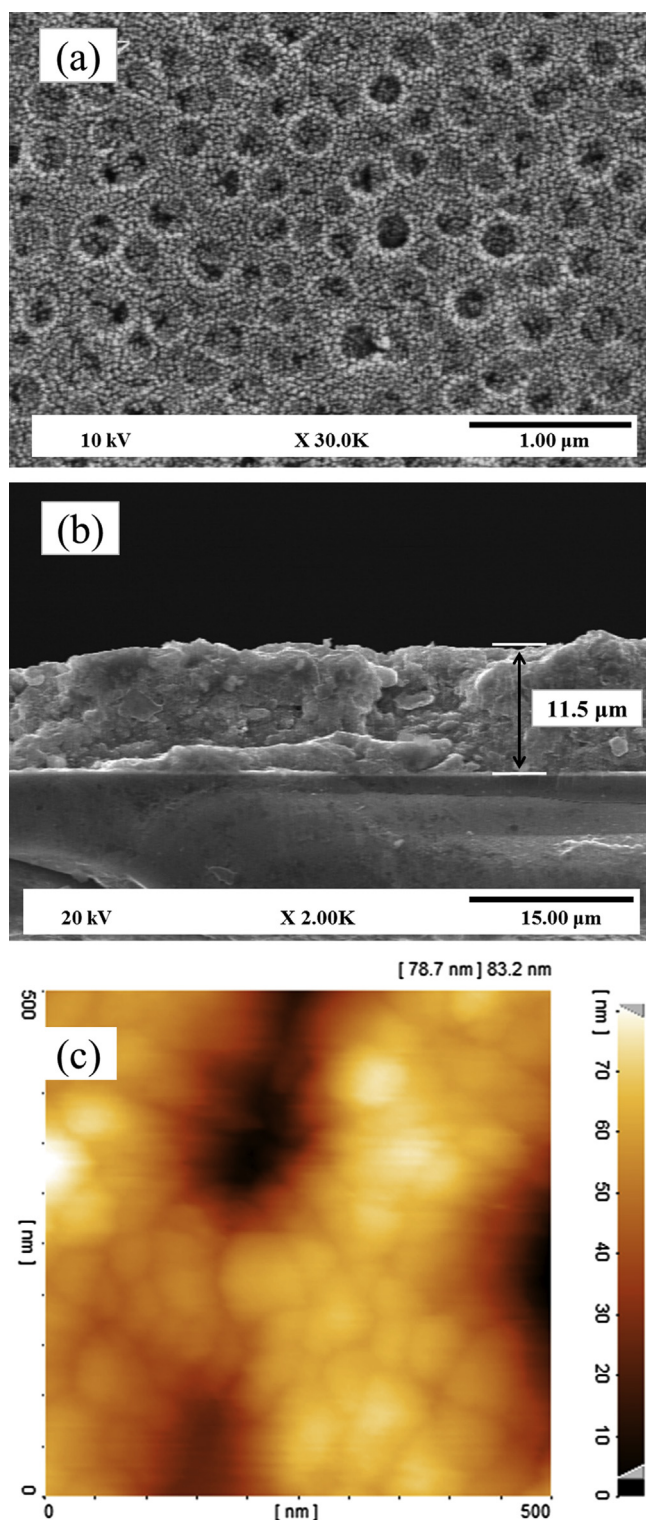

Fig. 5. (a) FESEM micrograph, (b) cross sectional view, and (c) AFM image of the hierarchical porous TiO_2 photoanode.
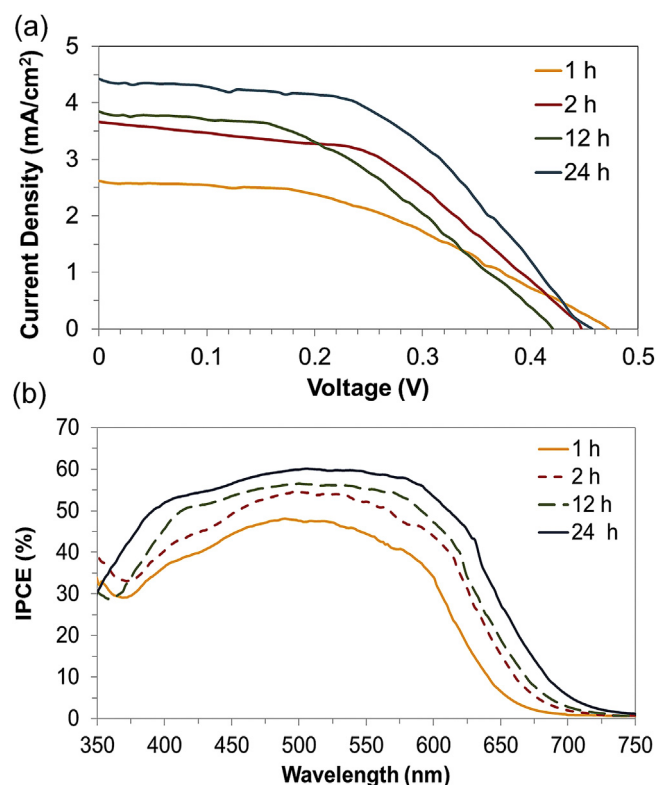

Fig. 6. (a) $J–V$ characteristic and (b) IPCE curves of QDSCs with QDs synthesized in different times.

more easily throughout the QRs, boosting the charge separation and injection. Furthermore, unlike the DSSCs, the photogenerated excitons in semiconductor nanoparticles should diffuse extra route before injection in QDSCs. The 1-dimensional route available in QRs greatly facilitates this process. In addition, the higher surface area of the QRs allows higher interfacial contact between particles and surrounding electrolyte, which further improves the charge separation [41]. On the other hand, smaller QDs penetrate further in porous photoanode under the same applied electrophoretic deposition voltage compared to the larger QRs or tetrapods. Although the presence of relatively large macro-channels in hierarchical porous structure guarantees the impregnation of all particles inside the porous photoanodes, QRs and tetrapods are deposited solely on upper layers. This implies the tandem rainbow structure solar cell with QDs with larger band gaps in lower layers and QRs and tetrapods with smaller band gaps in upper layers, which leads to a tremendous increase in absorption region and hence efficiency of the QDSC. This is schematically shown in Fig. S2 (Supplementary data).

The deposition of CdS buffer layer with SILAR causes enormous improvement in QDSC efficiency through (1) covering the TiO_2 surface and reducing the back reactions; (2) extending the absorption region as a co-sensitizer besides CdSe; (3) shifting

Table 1
J_{SC}, V_{OC}, FF, and η of QDSCs with QDs synthesized in various times.

Synthesis time	J_{SC} (mA cm^{-2})	V_{OC} (V)	FF	η (%)
1 h	2.65	0.46	0.47	0.57
2 h	3.70	0.45	0.50	0.83
12 h	3.90	0.42	0.50	0.82
24 h	4.48	0.45	0.52	1.05

downward the CB of TiO_2; and (4) providing the stepwise CB alignment between TiO_2 and CdSe, which assists the charge injection and hinders the back recombination [42,43]. Also, electron injection is faster in TiO_2/CdS compared to TiO_2/CdSe [44]. The ZnS over coating layer also passivates the surface traps, promotes the electron lifetime, and reduces the charge recombination at the QD/electrolyte interface [45]. The relatively wide peak in IPCE (Fig. 6(b)) is due to the tandem structure of the cell besides co-sensitization of CdS layer.

Although polysulfide (S^{2-}/S_n^{2-}) electrolyte has higher redox potential (-4.01 eV) compared to the Co^{2+}/Co^{3+} and OMeTAD [46], which leads to relatively lower V_{OC} in the QDSC, the high stability and diffusibility as well as compatibility with sulfide and seleno-sulfide species, introduce this electrolyte as a proper choice in QDSCs. On the other hand, the composite Cu_2S/CNT counter electrode provides faster electrolyte redox regeneration, which can further promote the QDSC efficiency. The higher performance of Cu_2S/graphene counter electrode was reported in QDSCs [47]. Therefore, the tandem structure of the cell, utilization of the QRs and tetrapods, co-sensitization with CdS buffer layer, ZnS blocking layer as well as Cu_2S/CNT counter electrode lead to the highest efficiency in QDSC with 24 h synthesized nanoparticles.

Fig. 7 shows the equivalent circuit, Nyquist plot, and Bode phase plot of the QDSCs with QDs synthesized at different times. In equivalent circuit, R_s is ohmic series resistance of the cell, R_{BL} and C_{BL} are charge transfer resistance and double layer capacitance at the interface of electrolyte and blocking layer, R_{CO} and C_{CO} are charge transfer resistance and double layer capacitance at FTO/TiO_2 interface, R_r and C_μ are charge transfer resistance and chemical capacitance at TiO_2/QD/electrolyte interface, R_t is resistivity of electron transport in TiO_2 film, Z_d is Warburg diffusion of redox couples in electrolyte, and R_{Cu2S} and C_{Cu2S} are charge transfer resistance and double layer capacitance at counter electrode. The equivalent circuit between R_s and Warburg diffusion can be simplified as parallel circuit of R_r and C_μ in high voltages [46]. The R_s values do not dramatically change (95–97 Ω), which shows nearly the same series resistance and electron transport behavior in all samples. However, the R_r value increases with decreasing the synthesis time. This demonstrates the higher recombination resistance in 12 and 24 h synthesized samples, which confirms the positive role of QRs in electron lifetime enhancement. The Bode phase plot (Fig. 7(c)) also reveals that the characteristic peak shifts to lower frequency with increasing the synthesis time. The characteristic peak frequency is related to the electron lifetime in TiO_2 matrix. This implies that the charge collection efficiency is enhanced in 24 h synthesized QD and QR containing QDSC, which might be due to the efficient role of QRs and tetrapods in charge separation and injection.

Finally, it should be noted that although the efficiency of these QDSCs is slightly lower compared to other QDSCs, it could be further improved by increasing the active area in hierarchical porous structure, improving the light management especially scattering the light in upper layers, and enhancing the surface coverage by QDs.

4. Conclusions

The CdSe QDs and QRs were successfully synthesized with various sizes, shapes, and crystalline phases by modified solvothermal method including spontaneous employment of stirring system and controlled applied internal pressure. The glorious synthesis temperature of 220 °C for 24 h leads to QDs with different sizes besides QRs and tetrapods. XRD and Raman curves confirmed the presence of ZB phase as the major phase and WZ as the minor one. The FTIR spectra showed almost all organic residues were removed after size selective separation. Also, the DRS data revealed the size quantization in both QDs and QRs. The hierarchical porous titania photoanode with macropore sizes of 350 nm and mesopore sizes of 25 nm was synthesized. QDSC based on 24 h synthesize QDs and QRs exhibited the best performance among all synthesis times. Not only the hierarchical porous titania photoanode, the composite CNT/Cu_2S cathode, and electrophoretic deposition of QDs and QRs, but also the co-sensitization of CdS and CdSe, the tandem structure of various CdSe shapes, and beneficial role of QRs have led to the tremendous increase in device performance.

Appendix A. Supplementary data

Supplementary data related to this article can be found at http://dx.doi.org/10.1016/j.jpowsour.2014.01.055.
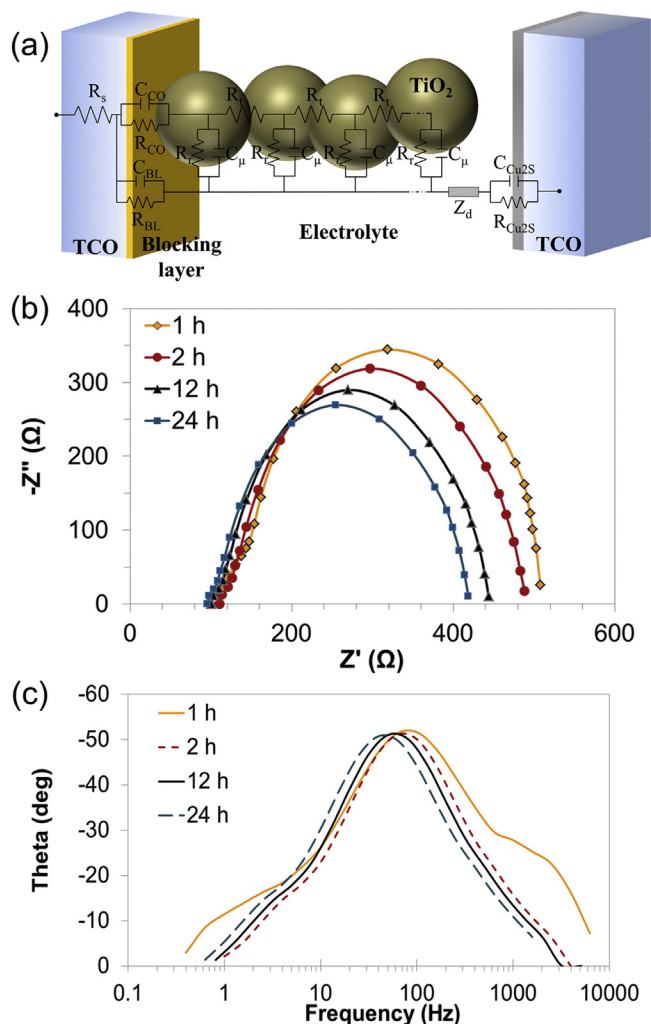

Fig. 7. (a) Equivalent circuit, (b) Nyquist plot, and (c) Bode phase plot of QDSCs with QDs synthesized at different times.

References

[1] M. Grätzel, Nature 414 (2001) 338–344.
[2] A. Hagfeldt, G. Boschloo, L. Sun, L. Kloo, H. Pettersson, Chem. Rev. 110 (2010) 6595–6663.
[3] I. Chung, B. Lee, J. He, R.P.H. Chang, M.G. Kanatzidis, Nature 485 (2012) 486–489.
[4] B.E. Hardin, H.J. Snaith, M.D. McGehee, Nat. Photonics 6 (2012) 162–169.
[5] L.M. Peter, J. Phys. Chem. Lett. 2 (2011) 1861–1867.
[6] I.J. Kramer, E.H. Sargent, ACS Nano 5 (2011) 8506–8514.
[7] P.V. Kamat, J. Phys. Chem. C 112 (2008) 18737–18753.
[8] P.V. Kamat, K. Tvrdy, D.R. Baker, J.G. Radich, Chem. Rev. 110 (2010) 6664–6688.
[9] M.C. Beard, J. Phys. Chem. Lett. 2 (2011) 1282–1288.
[10] J.W. Lee, D.Y. Son, T.K. Ahn, H.W. Shin, I.Y. Kim, S.J. Hwang, M.J. Ko, S. Sul, H. Han, N.G. Park, Sci. Rep. 3 (2013), http://dx.doi.org/10.1038/srep01050.
[11] I. Hod, V. Gonzalez-Pedro, Z. Tachan, F. Fabregat-Santiago, I. Mora-Sero, J. Bisquert, A. Zaban, J. Phys. Chem. Lett. 2 (2011) 3032–3035.
[12] E.M. Barea, M. Shalom, S. Gimenez, I. Hod, I. Mora-Sero, A. Zaban, J. Bisquert, J. Am. Chem. Soc. 132 (2010) 6834–6839.
[13] V. Chakrapani, D. Baker, P.V. Kamat, J. Am. Chem. Soc. 133 (2011) 9607–9615.
[14] G.S. Paul, J.H. Kim, M.S. Kim, K. Do, J. Ko, J.S. Yu, Appl. Mater. Interfaces 4 (2012) 375–381.
[15] N. Guijarro, T. Lana-Villarreal, I. Mora-Sero, J. Bisquert, R. Gomez, J. Phys. Chem. C 113 (2009) 4208–4214.
[16] M.A. Green, K. Emery, Y. Hishikawa, W. Warta, E.D. Dunlop, Prog. Photovolt. Res. Appl. 21 (2013) 1–11.
[17] K. Lee, S.W. Park, M.J. Ko, K. Kim, N.G. Park, Nat. Mater. 8 (2009) 665–671.
[18] P.K. Santra, P.V. Kamat, J. Am. Chem. Soc. 135 (2013) 877–885.
[19] H.J. Lee, J.H. Yum, H.C. Leventis, S.M. Zakeeruddin, S.A. Haque, P. Chen, S.I. Seok, M. Grätzel, Md. K. Nazeeruddin, J. Phys. Chem. C 112 (2008) 11600–11608.
[20] A. Kongkanand, K. Tvrdy, K. Takechi, M. Kuno, P.V. Kamat, J. Am. Chem. Soc. 130 (2008) 4007–4015.
[21] A. Salant, M. Shalom, I. Hod, A. Faust, A. Zaban, U. Banin, ACS Nano 4 (2010) 5962–5968.
[22] Q. Zhang, X. Guo, X. Huang, S. Huang, D. Li, Y. Luo, Q. Shen, T. Toyoda, Q. Meng, Phys. Chem. Chem. Phys. 13 (2011) 4659–4667.
[23] M. Samadpour, S. Giménez, P.P. Boix, Q. Shen, M.E. Calvo, N. Taghavinia, A. Irajizad, T. Toyoda, H. Miguez, I. Mora-Sero, Electrochim. Acta 75 (2012) 139–145.
[24] Y. Li, H. Liao, Y. Ding, Y. Fan, Y. Zhang, Y. Qian, Inorg. Chem. 38 (1999) 1382–1387.
[25] K.B. Tang, Y.T. Qian, J.H. Zeng, X.G. Yang, Adv. Mater. 15 (2003) 448–450.
[26] X. Wang, Z. Feng, D. Fan, F. Fan, C. Li, Cryst. Growth Des. 10 (2010) 5312–5318.
[27] M. Soreni-Harari, N. Yaacobi-Gross, D. Steiner, A. Aharoni, U. Banin, O. Millo, N. Tessler, Nano Lett. 8 (2008) 678–684.
[28] X. Peng, L. Manna, W. Yang, J. Wickham, E. Scher, A. Kadavanich, A.P. Alivisatos, Nature 54 (2000) 59–61.
[29] L. Manna, E.C. Scher, A.P. Alivisatos, J. Am. Chem. Soc. 122 (2000) 12700–12706.
[30] P. Innocenzi, L. Malfatti, G.J.A.A. Soler-Illia, Chem. Mater. 23 (2011) 2501–2509.
[31] M.R. Golobostanfard, H. Abdizadeh, Ceram. Int. 38 (2012) 5843–5851.
[32] M.R. Golobostanfard, H. Abdizadeh, Microporous Mesoporous Mater. 183 (2014) 74–80.
[33] H. Chu, X. Li, G. Chen, W. Zhou, Y. Zhang, Z. Jin, J. Xu, Y. Li, Cryst. Growth Des. 5 (2005) 1801–1806.
[34] R. Venugopal, P. Lin, C.C. Liu, Y.T. Chen, J. Am. Chem. Soc. 127 (2005) 11262–11268.
[35] S.J. Rosenthal, J. McBride, S.J. Pennycook, L.C. Feldman, Surf. Sci. Rep. 62 (2007) 111–157.
[36] D.V. Talapin, J.S. Lee, M.V. Kovalenko, E.V. Shevchenko, Chem. Rev. 110 (2010) 389–458.
[37] Q. Pang, L. Zhao, Y. Cai, D.P. Nguyen, N. Regnault, N. Wang, S. Yang, W. Ge, R. Ferreira, G. Bastard, J. Wang, Chem. Mater. 17 (2005) 5263–5267.
[38] B. Zorman, M.V. Ramakrishna, R.A. Friesner, J. Phys. Chem. 99 (1995) 7649–7653.
[39] S. Ruhle, M. Shalom, A. Zaban, Chem. Phys. Chem. 11 (2010) 2290–2304.
[40] A. Salant, M. Shalom, Z. Tachan, S. Buhbut, A. Zaban, U. Banin, Nano Lett. 12 (2012) 2095–2100.
[41] P.V. Kamat, Acc. Chem. Res. 45 (2012) 1906–1915.
[42] Y.L. Lee, Y.S. Lo, Adv. Funct. Mater. 19 (2009) 604–609.
[43] I. Mora-Sero, J. Bisquert, J. Phys. Chem. Lett. 1 (2010) 3046–3052.
[44] S. Emin, M. Yanagida, W. Peng, L. Han, Sol. Energy Mater. Sol. C 101 (2012) 5–10.
[45] N. Guijarro, J.M. Campina, Q. Shen, T. Toyoda, T. Lana-Villarreala, R. Gomez, Phys. Chem. Chem. Phys. 13 (2011) 12024–12032.
[46] F. Fabregat-Santiago, G. Garcia-Belmonte, I. Mora-Sero, J. Bisquert, Phys. Chem. Chem. Phys. 13 (2011) 9083–9118.
[47] J.G. Radich, R. Dwyer, P.V. Kamat, J. Phys. Chem. Lett. 2 (2011) 2453–2460.